



**HAL**  
open science

## Mid-infrared emission properties of erbium-doped fluorite-type crystals

Simone Normani, Pavel Loiko, Liza Basyrova, Abdelmjid Benayad, Alain Braud, Elena Dunina, Liudmila Fomicheva, Alexey Kornienko, Ammar Hideur, Patrice Camy

► **To cite this version:**

Simone Normani, Pavel Loiko, Liza Basyrova, Abdelmjid Benayad, Alain Braud, et al.. Mid-infrared emission properties of erbium-doped fluorite-type crystals. *Optical Materials Express*, 2023, 13 (7), pp.1836-1851. 10.1364/OME.482402. hal-04209389

**HAL Id: hal-04209389**

**<https://hal.science/hal-04209389v1>**

Submitted on 1 Nov 2023

**HAL** is a multi-disciplinary open access archive for the deposit and dissemination of scientific research documents, whether they are published or not. The documents may come from teaching and research institutions in France or abroad, or from public or private research centers.

L'archive ouverte pluridisciplinaire **HAL**, est destinée au dépôt et à la diffusion de documents scientifiques de niveau recherche, publiés ou non, émanant des établissements d'enseignement et de recherche français ou étrangers, des laboratoires publics ou privés.

# Mid-infrared emission properties of erbium-doped fluorite-type crystals

SIMONE NORMANI,<sup>1</sup> PAVEL LOIKO,<sup>1</sup> LIZA BASYROVA,<sup>1</sup> ABDELMJID BENAYAD,<sup>1</sup> ALAIN BRAUD,<sup>1</sup> ELENA DUNINA,<sup>2</sup> LIUDMILA FOMICHEVA,<sup>3</sup> ALEXEY KORNIENKO,<sup>2</sup> AMMAR HIDEUR,<sup>4</sup> AND PATRICE CAMY<sup>1,\*</sup>

<sup>1</sup>Centre de Recherche sur les Ions, les Matériaux et la Photonique (CIMAP), UMR 6252 CEA-CNRS-ENSICAEN, Université de Caen Normandie, 6 Boulevard Maréchal Juin, 14050 Caen Cedex 4, France

<sup>2</sup>Vitebsk State Technological University, 210035 Vitebsk, Belarus

<sup>3</sup>Belarusian State University of Informatics and Radioelectronics, 6 Brovka St., 220027, Minsk, Belarus

<sup>4</sup>CORIA UMR6614, CNRS-INSA-Université de Rouen, Normandie Université, Avenue de l'université, BP. 12, 76801 Saint Etienne du Rouvray, France

\*patrice.camy@ensicaen.fr

**Abstract:** We report on a comparative study of the spectroscopic properties and mid-infrared laser performance of five 5 at.% Er<sup>3+</sup>-doped fluorite-type crystals MF<sub>2</sub>, including parent compounds CaF<sub>2</sub>, SrF<sub>2</sub>, BaF<sub>2</sub>, and solid-solution (“mixed”) ones (Ca,Sr)F<sub>2</sub> and (Sr,Ba)F<sub>2</sub>. In the M = Ca → Sr → Ba series, the host matrix phonon energy decreases, the absorption and mid-infrared emission spectra of Er<sup>3+</sup> become narrower and more structured, and the luminescence lifetimes of the <sup>4</sup>I<sub>11/2</sub> and <sup>4</sup>I<sub>13/2</sub> Er<sup>3+</sup> manifolds increase. The Er<sup>3+</sup> transition probabilities were calculated using the Judd-Ofelt theory. In the “mixed” compounds, the Er<sup>3+</sup> ions tend to reside in the larger / heavier cation environment. The low-temperature (12 K) spectroscopy evidences the presence of a single type of clusters at this doping level; the crystal-field splitting for Er<sup>3+</sup> ions in clusters was determined. Continuous-wave low-threshold laser operation at ~2.8 μm (the <sup>4</sup>I<sub>11/2</sub> → <sup>4</sup>I<sub>13/2</sub> transition) was achieved with all five Er<sup>3+</sup>:MF<sub>2</sub> crystals. The maximum achieved laser slope efficiency was 37.9% (Er<sup>3+</sup>:CaF<sub>2</sub>), 23.5% (Er<sup>3+</sup>:SrF<sub>2</sub>) and 17.2% (Er<sup>3+</sup>:BaF<sub>2</sub>).

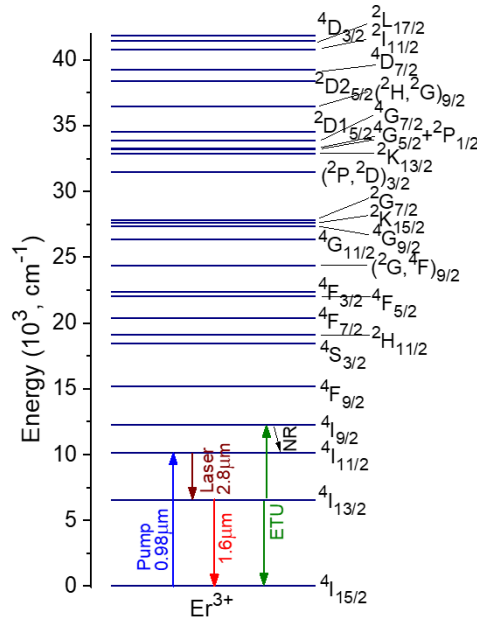
© 2022 Optica Publishing Group under the terms of the [Optica Publishing Group Open Access Publishing Agreement](#)

## 1. Introduction

Calcium fluoride (CaF<sub>2</sub>, also known as fluorite in the mineral form) is a well-known laser host material for doping with trivalent rare-earth ions (RE<sup>3+</sup>) [1-3]. Undoped CaF<sub>2</sub> features good thermal properties (high thermal conductivity and isotropic thermal expansion), low phonon energy, low refractive index and broadband transparency. It also exhibits a unique tendency for strong RE<sup>3+</sup> ion clustering even at moderate doping concentrations (>0.1 at.%), leading to inhomogeneously broadened spectral bands [4-6]. As a result, the absorption and emission spectra of RE<sup>3+</sup> ions in CaF<sub>2</sub> greatly resemble those in fluoride glasses being almost structureless and very broad. Such a “glassy-like” spectroscopic behavior is very appealing for broadband wavelength tuning [7,8] and generation of ultrashort pulses in mode-locked lasers [9,10]. The energy-transfer processes among the neighboring RE<sup>3+</sup> ions (nonradiative energy-transfer, cross-relaxation, and energy-transfer upconversion) are greatly promoted in clusters [11]. This can be used for boosting the efficiency of certain laser transitions of RE<sup>3+</sup> ions. CaF<sub>2</sub> is a low-melting-point compound. Its growth is well-developed, e.g., by the Czochralski or Bridgman-Stockbarger methods.

CaF<sub>2</sub> belongs to the family of divalent metal fluorides, MF<sub>2</sub> (where M = Ca, Sr, Ba, Cd, or Pb) [12-15]. These materials all belong to the cubic class (sp. gr. *Fm*3<sup>-</sup>*m*, fluorite-type structure). The M<sup>2+</sup> and F<sup>-</sup> are located at face-centered cubic lattice points and tetrahedral voids, respectively. Compared to CaF<sub>2</sub>, other MF<sub>2</sub> crystals are less studied for RE<sup>3+</sup> doping but they are also attractive as laser host media as they benefit from either a lower melting point, or better

47 thermal properties, or lower phonon energies. Fluorite-type crystals can also form substitutional  
 48 solid-solutions  $(M1_{1-x}M2_x)F_2$  for the entire range of  $0 < x < 1$  [16-18]. For such “mixed”  
 49 compositions, the melting point is expected to decrease further as compared to the parent  
 50 compounds [19,20]. An additional spectral broadening is also expected due to the compositional  
 51 disorder. The growth and laser operation of some  $RE^{3+}$ -doped “mixed” fluorite-type crystals  
 52 were reported mainly focusing on  $(Ca,Sr)F_2$  [21-23].



53  
 54 **Fig. 1.** Energy level scheme of  $Er^{3+}$  ions showing all the manifolds assigned in the absorption  
 55 spectra of  $Er^{3+}:MF_2$  crystals, pump and laser transitions, ETU – energy-transfer upconversion.

53

54

55

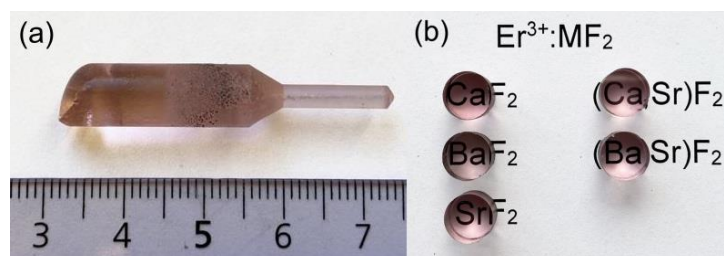
56 Erbium ions ( $Er^{3+}$ ) are of interest for generation of mid-infrared radiation at  $\sim 2.8 \mu\text{m}$  [24,25]  
 57 according to the  $4I_{11/2} \rightarrow 4I_{13/2}$  transition, Fig. 1. The low-phonon-energy behavior of  $MF_2$  crystals  
 58 and the tendency for strong ion clustering promoting the energy-transfer upconversion stimulate  
 59 the interest in the development of mid-infrared  $Er^{3+}:MF_2$  lasers. Labbe *et al.* first reported on a  
 60 mid-infrared 5 at.%  $Er^{3+}:CaF_2$  laser delivering 80 mW at  $2.80 \mu\text{m}$  with a slope efficiency of 30%  
 61 and a small laser threshold of 23 mW [1]. Basyrova *et al.* demonstrated power scaling of a similar  
 62 laser generating 0.83 W at  $2.80 \mu\text{m}$  with a slightly higher slope efficiency of 31.6% [26]. In  
 63 these studies, high-brightness laser pumping was implemented. Further power scaling was  
 64 achieved using commercial InGaAs diode lasers as pump sources. Zong *et al.* developed a  
 65 diode-pumped 1.7 at.%  $Er^{3+}:CaF_2$  laser generating 2.32 W at  $2.76 \mu\text{m}$  at the expense of a lower  
 66 slope efficiency of 21.2% [27]. So far,  $Er^{3+}:CaF_2$  [26,27],  $Er^{3+}:SrF_2$  [28] and  $Er^{3+}:(Ca,Sr)F_2$  [23]  
 67 crystals have been studied for mid-infrared lasers. Note that  $Er^{3+}:CaF_2$  can also be obtained in  
 68 the form of transparent ceramics. Šulc *et al.* reported on a pulsed diode-pumped 5 at.%  $Er^{3+}:CaF_2$   
 69 ceramic laser with a broad tuning range of 2687 – 2805 nm (118 nm) [29].

70 Despite the existence of multiple studies for several  $Er^{3+}:MF_2$  crystal compositions, their  
 71 spectroscopic and mid-infrared laser properties have not been directly compared so far. In the  
 72 present work, we report on a comparative study of mid-infrared emission properties of five  
 73 fluorite-type  $Er^{3+}$ -doped  $MF_2$  crystals, including parent and solid-solution compounds.

## 74 2. Crystal growth

75 The  $MF_2$  crystals ( $M = Ca, Sr, Ba$ ) melt congruently at relatively low temperatures (cf. Table 1)  
 76 and they can be grown by the Bridgman-Stockbarger or Czochralski methods. The  $Er^{3+}:MF_2$   
 77 crystals were grown by the Bridgman method using graphite crucibles ( $\Phi 7\text{-}8 \text{ mm}$ , height: 40

78 mm). The MF<sub>2</sub> (M = Ca, Sr, Ba) powders (purity: 4N, Sigma-Aldrich) and ErF<sub>3</sub> powder obtained  
 79 by fluorination of the Er<sub>2</sub>O<sub>3</sub> precursor (4N, Alfa Aesar). Five compositions were tested: M = Ca,  
 80 Sr, Ba, Ca<sub>0.5</sub>Sr<sub>0.5</sub> and Sr<sub>0.5</sub>Ba<sub>0.5</sub>. The doping level was 5 at.% Er<sup>3+</sup> (with respect to M<sup>2+</sup> cations).  
 81 The optical quality and spectroscopic properties of RE<sup>3+</sup>-doped MF<sub>2</sub> crystals are sensitive to  
 82 even small pollution of oxygen / water in the growth chamber as they can lead to the presence  
 83 of oxygen-assisted sites for the dopant ions or even formation of a translucent oxyfluoride phase.  
 84 To avoid that, the growth chamber was sealed to vacuum (<10<sup>-5</sup> mbar) and refilled with a mixture  
 85 of Ar + CF<sub>4</sub> gases. The starting reagents were well mixed and placed into the crucible which was  
 86 then heated slightly above (~30-50 °C) the melting point and the solution was homogenized for  
 87 3-4 hours (h). The growth was ensured by a vertical translation of the crucible in a vertical  
 88 temperature gradient of 30-40 °C/cm. After the growth was completed, the crystals were cooled  
 89 down to room temperature (20 °C) within 48 h.



90  
 91 **Fig. 2.** Photographs of Er<sup>3+</sup>:MF<sub>2</sub> crystals: (a) an as-grown Er<sup>3+</sup>:CaF<sub>2</sub> crystal boule; (b) cut and  
 92 polished Er<sup>3+</sup>:MF<sub>2</sub> samples.

93 For the “mixed” crystals, the melting point is reduced as compared to those of the parent  
 94 compounds. E.g., for Er<sup>3+</sup>:(Ca,Sr)F<sub>2</sub> and Er<sup>3+</sup>:(Sr,Ba)F<sub>2</sub>, it is  $T_f = 1373$  °C and  $1315$  °C,  
 95 respectively (compare with  $1477$  °C,  $1418$  °C and  $1386$  °C for SrF<sub>2</sub>, CaF<sub>2</sub> and BaF<sub>2</sub>,  
 96 respectively).

97 The as-grown Er<sup>3+</sup>:MF<sub>2</sub> crystals with a cylindrical shape ( $\Phi 7-8$  mm, length: 35 - 40 mm)  
 98 were transparent and rose-colored due to the Er<sup>3+</sup> doping, Fig. 2(a). Samples for spectroscopic  
 99 and laser studies were cut from the central part of the cylindrical barrels with a thickness of 6-7  
 100 mm and then polished to laser-grade quality, Fig. 2(b).

### 101 3. Raman spectra

102 The Raman spectra of Er<sup>3+</sup>:MF<sub>2</sub> crystals, Fig. 3(a), were measured using a confocal microscope  
 103 (InVia, Renishaw) equipped with a  $\times 50$  Leica objective and an Ar<sup>+</sup> ion laser (457 nm). Fluorite-  
 104 type crystals have O<sub>h</sub> symmetry and a triatomic unit cell thus exhibiting only one Raman-active  
 105 mode at the center of the Brillouin zone having a T<sub>2g</sub> symmetry [30]. Indeed, the Raman spectra  
 106 of all the studied Er<sup>3+</sup>:MF<sub>2</sub> crystals contain a single intense peak assigned to this vibration.  
 107 Frequently, MF<sub>2</sub> crystals may exhibit additional broad Raman bands in the spectral range of 100  
 108 – 600 cm<sup>-1</sup> owing to structure defects (interstitial / vacant anion sites) [30]. Such a behavior is  
 109 not observed in our crystals.

110 For Er<sup>3+</sup>:CaF<sub>2</sub>, Er<sup>3+</sup>:SrF<sub>2</sub> and Er<sup>3+</sup>:BaF<sub>2</sub> crystals, the peak frequency of the Raman mode and  
 111 its linewidth (FWHM) are 321 / 11.0 cm<sup>-1</sup>, 285 / 10.2 cm<sup>-1</sup> and 242 / 12.0 cm<sup>-1</sup>, respectively.  
 112 Thus, the latter compound is the most favorable one in terms of low-phonon-energy behavior.  
 113 For the “mixed” compositions, the Raman peak broadens and is reduced in intensity and the peak  
 114 position takes an intermediate place between those for the corresponding parent compounds,  
 115 indicating an even distribution of the host-forming cations throughout the structure (a formation  
 116 of a substitutional solid-solution) [32]. E.g., for Er<sup>3+</sup>:(Ca,Sr)F<sub>2</sub>, the peak Raman frequency is 304  
 117 cm<sup>-1</sup> and the peak linewidth is 25.9 cm<sup>-1</sup>.

118 The phonon energy of Er<sup>3+</sup>:MF<sub>2</sub> decreased monotonically with increasing the cationic mass  
 119 in agreement with the classical approach,  $\nu = (1/2\pi)(k/\mu)^{1/2}$ , where  $k$  is the force constant and  $\mu$   
 120 is the reduced mass of the M – F system [33].

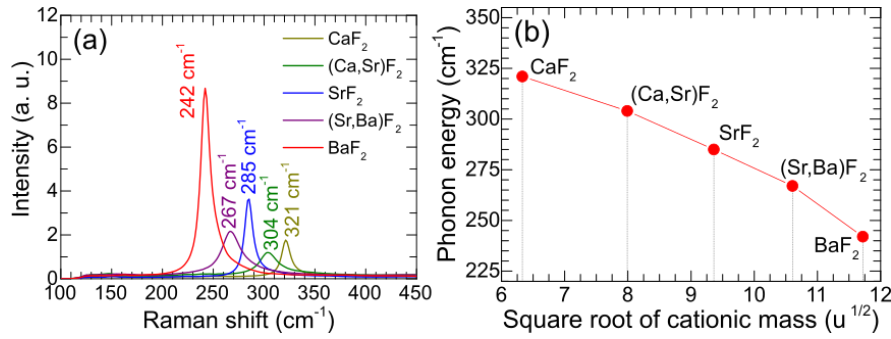


**Fig. 3.** Raman spectroscopy of Er<sup>3+</sup>:MF<sub>2</sub> crystals: (a) Raman spectra,  $\lambda_{\text{exc}} = 457 \text{ cm}^{-1}$ , numbers – peak frequencies; (b) phonon energy vs. the square root of the average cationic mass.

121  
122  
123

#### 4. Optical spectroscopy

124

##### 4.1 Optical absorption

125

126 The absorption spectra of Er<sup>3+</sup> ions were measured using a spectrophotometer (Lambda 1050,  
127 Perkin Elmer). They are shown in Fig. 4. Here, the assignment of Er<sup>3+</sup> transitions is according  
128 to Carnall *et al.* [34]. The absorption spectra for both parent and “mixed” Er<sup>3+</sup>:MF<sub>2</sub> crystals are  
129 smooth and broad owing to inhomogeneous spectral broadening caused by a strong ion  
130 clustering. In the series M = Ca → Sr → Ba, the complexity and diversity of RE<sup>3+</sup> ion clusters  
131 in MF<sub>2</sub> crystals decrease leading to more intense and structured absorption bands which also  
132 exhibit a slight blue-shift [12]. Indeed, for the <sup>4</sup>I<sub>15/2</sub> → <sup>4</sup>I<sub>11/2</sub> transition, which is used for pumping  
133 mid-infrared erbium lasers, the peak absorption cross-section,  $\sigma_{\text{abs}}$ , varies from  $2.77 \times 10^{-21} \text{ cm}^2$   
134 at 972.3 nm (Er<sup>3+</sup>:BaF<sub>2</sub>) to  $2.59 \times 10^{-21} \text{ cm}^2$  at 969.5 nm (Er<sup>3+</sup>:SrF<sub>2</sub>), to  $2.22 \times 10^{-21} \text{ cm}^2$  at 967.6  
135 nm (Er<sup>3+</sup>:CaF<sub>2</sub>), while the corresponding absorption bandwidth is 12.9 nm (Er<sup>3+</sup>:BaF<sub>2</sub>), 16.9 nm  
136 (Er<sup>3+</sup>:SrF<sub>2</sub>), and 22.2 nm (Er<sup>3+</sup>:CaF<sub>2</sub>).

137

A close look at the absorption spectra of “mixed” crystals indicate that there is a great  
138 similarity between those of (Er<sup>3+</sup>:(Ca,Sr)F<sub>2</sub> and Er<sup>3+</sup>:SrF<sub>2</sub>) and (Er<sup>3+</sup>:(Sr,Ba)F<sub>2</sub> and Er<sup>3+</sup>:BaF<sub>2</sub>)  
139 ones, suggesting that the dopant ions in such solid-solution compounds tend to reside in clusters  
140 with a local surrounding predominantly composed of one of the two host-forming cations  
141 (namely, the heavier / larger one – Sr<sup>2+</sup> or Ba<sup>2+</sup>, respectively). This suggests that Er<sup>3+</sup> clusters  
142 have a tendency to sit in the heavier-cation environment within the solid-solution (M<sub>1-x</sub>M<sub>2-x</sub>)F<sub>2</sub>  
143 crystals. A similar behavior was observed previously for clusters of Nd<sup>3+</sup>/Lu<sup>3+</sup> ions in “mixed”  
144 (Sr,Ba)F<sub>2</sub> crystals [35].

145

##### 4.2 Judd-Ofelt analysis

146

The measured absorption spectra of Er<sup>3+</sup> ions in the five studied MF<sub>2</sub> crystals were used to  
147 calculate the transition probabilities by means of the standard Judd-Ofelt (J-O) theory [36,37].  
148 The reduced squared matrix elements  $U^{(k)}$  ( $k = 2, 4, 6$ ) were calculated using the free-ion  
149 parameters from [38]. The magnetic dipole (MD) contributions to transition intensities (for  
150  $\Delta J = J - J' = 0, \pm 1$ ) were calculated within the Russell–Saunders approximation using Er<sup>3+</sup> wave  
151 functions under the free-ion assumption.

152

Table 1 summarizes the experimental and calculated absorption oscillator strengths ( $f_{\text{exp}}$  and  
153  $f_{\text{calc}}$ , respectively) for the three parent compounds, Er<sup>3+</sup>:CaF<sub>2</sub>, Er<sup>3+</sup>:SrF<sub>2</sub> and Er<sup>3+</sup>:BaF<sub>2</sub>. There  
154 exists a direct relation between the absorption oscillator strength / integrated absorption cross-  
155 section and the radiative lifetime of the excited-state (the principle of reciprocity, referring to  
156 Einstein coefficients). For Er<sup>3+</sup> transitions from the ground-state (<sup>4</sup>I<sub>15/2</sub>) to the two lower-lying  
157 excited-states (<sup>4</sup>I<sub>13/2</sub> and <sup>4</sup>I<sub>11/2</sub>), the  $f_{\text{calc}}$  value decreases in the M = Ca → Sr → Ba series, so that  
158 an opposite tendency is expected for the radiative lifetimes of these two states. The root mean  
159 square (r.m.s.) deviation between the  $f_{\text{exp}}$  and  $f_{\text{calc}}$  values is relatively low for all the tested  
160 Er<sup>3+</sup>:MF<sub>2</sub> crystals, lying in the range of 0.137 – 0.257.

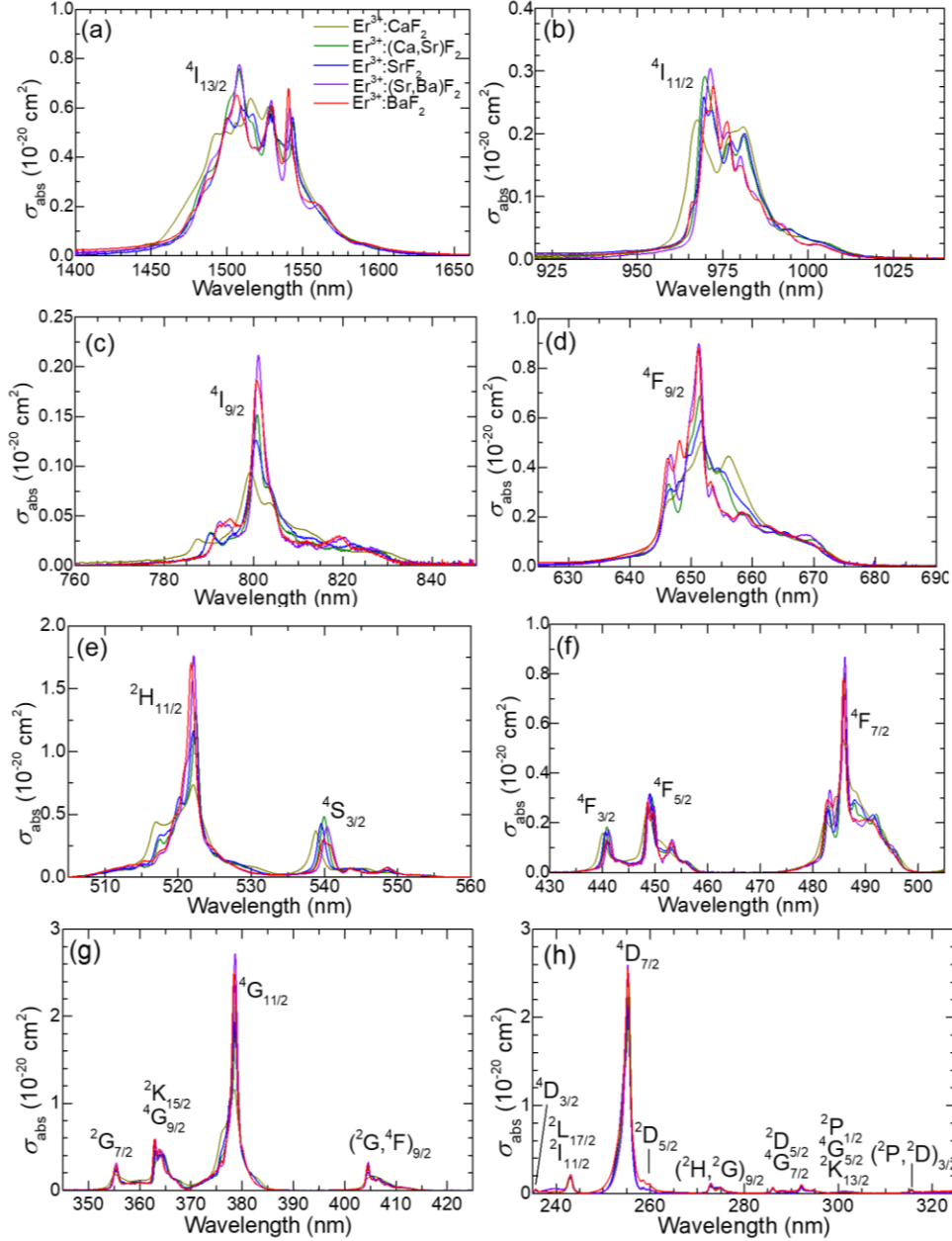


**Fig. 4.** (a-h) Absorption spectra of Er<sup>3+</sup> ions in MF<sub>2</sub> crystals.

161

162

The J-O (intensity) parameters  $\Omega_2$ ,  $\Omega_4$ ,  $\Omega_6$  for Er<sup>3+</sup> ions in MF<sub>2</sub> crystals are listed in Table 2.

163

The determined J-O parameters were used to calculate the probabilities of spontaneous radiative transitions of Er<sup>3+</sup> ions. In Table 3, we list the parameters relevant for mid-infrared laser operation, i.e., the radiative lifetimes  $\tau_{\text{rad}}$  of the <sup>4</sup>I<sub>13/2</sub> and <sup>4</sup>I<sub>11/2</sub> states and the luminescence branching ratio  $\beta_{JJ'}$  for the <sup>4</sup>I<sub>11/2</sub> → <sup>4</sup>I<sub>13/2</sub> transition. As expected, in the M = Ca → Sr → Ba series, the  $\tau_{\text{rad}}$  values for the considered excited-states tend to increase from 7.09 / 6.53 ms (Er<sup>3+</sup>:CaF<sub>2</sub>) to 7.57 / 6.99 ms (Er<sup>3+</sup>:SrF<sub>2</sub>) and further to 7.52 / 7.11 ms (Er<sup>3+</sup>:BaF<sub>2</sub>). The considered  $\beta_{JJ'}$  value is also higher for Sr<sup>2+</sup> and Ba<sup>2+</sup>-containing crystals.

164

165

166

167

168

169

170

171

**Table 1. Absorption Oscillator Strengths<sup>a</sup> for Er<sup>3+</sup> Ions in Parent MF<sub>2</sub> (M = Ca, Sr, Ba) Crystals**

Transition	Er <sup>3+</sup> :CaF <sub>2</sub>		Er <sup>3+</sup> :SrF <sub>2</sub>		Er <sup>3+</sup> :BaF <sub>2</sub>	
	$f_{\text{exp}}, \times 10^{-6}$	$f_{\text{calc}}, \text{J-O}, \times 10^{-6}$	$f_{\text{exp}}, \times 10^{-6}$	$f_{\text{calc}}, \text{J-O}, \times 10^{-6}$	$f_{\text{exp}}, \times 10^{-6}$	$f_{\text{calc}}, \text{J-O}, \times 10^{-6}$
<sup>4</sup> I <sub>15/2</sub> → <sup>2S+1</sup> L <sub>J</sub>						
<sup>4</sup> I <sub>13/2</sub>	2.496	1.643 <sup>ED</sup> + 0.448 <sup>MD</sup>	2.129	1.510 <sup>ED</sup> + 0.448 <sup>MD</sup>	2.220	1.404 <sup>ED</sup> + 0.461 <sup>MD</sup>
<sup>4</sup> I <sub>11/2</sub>	0.714	0.693 <sup>ED</sup>	0.643	0.631 <sup>ED</sup>	0.598	0.592 <sup>ED</sup>
<sup>4</sup> I <sub>9/2</sub>	0.333	0.229 <sup>ED</sup>	0.328	0.283 <sup>ED</sup>	0.343	0.333 <sup>ED</sup>
<sup>4</sup> F <sub>9/2</sub>	2.264	2.139 <sup>ED</sup>	2.217	2.283 <sup>ED</sup>	2.265	2.406 <sup>ED</sup>
<sup>4</sup> S <sub>3/2</sub> + <sup>2</sup> H <sub>11/2</sub>	3.531	3.366 <sup>ED</sup>	3.422	3.544 <sup>ED</sup>	4.387	4.760 <sup>ED</sup>
<sup>4</sup> F <sub>7/2</sub>	2.141	2.454 <sup>ED</sup>	2.396	2.342 <sup>ED</sup>	2.205	2.236 <sup>ED</sup>
<sup>4</sup> F <sub>5/2</sub> + <sup>2</sup> F <sub>3/2</sub>	1.266	1.300 <sup>ED</sup>	1.114	1.173 <sup>ED</sup>	0.962	1.056 <sup>ED</sup>
<sup>2</sup> G <sub>9/2</sub>	0.898	0.970 <sup>ED</sup>	0.637	0.902 <sup>ED</sup>	0.603	0.840 <sup>ED</sup>
<sup>4</sup> G <sub>11/2</sub> + <sup>2</sup> K <sub>15/2</sub> + <sup>4</sup> G <sub>9/2</sub> + <sup>2</sup> G <sub>7/2</sub>	7.888	7.917 <sup>ED</sup> + 0.053 <sup>MD</sup>	8.585	8.474 <sup>ED</sup> + 0.053 <sup>MD</sup>	11.400	11.168 <sup>ED</sup> + 0.055 <sup>MD</sup>
r.m.s. dev.		0.217		0.137		0.234

172  
173

<sup>a</sup> $f_{\text{exp}}$  and  $f_{\text{calc}}$  - experimental and calculated absorption oscillator strengths, respectively, ED – electric dipole, MD – magnetic dipole.

174

**Table 2. Judd-Ofelt Parameters of Er<sup>3+</sup> Ions in MF<sub>2</sub> Crystals**

Host crystal	$\Omega_2, 10^{-20} \text{ cm}^2$	$\Omega_4, 10^{-20} \text{ cm}^2$	$\Omega_6, 10^{-20} \text{ cm}^2$
CaF <sub>2</sub>	1.436	1.364	1.892
(Ca,Sr)F <sub>2</sub>	1.244	1.483	1.720
SrF <sub>2</sub>	1.477	1.701	1.701
(Sr,Ba)F <sub>2</sub>	1.519	1.836	1.529
BaF <sub>2</sub>	2.397	1.964	1.487

175

**Table 3. Selected Probabilities<sup>a</sup> of Spontaneous Radiative Transitions of Er<sup>3+</sup> in MF<sub>2</sub> crystals**

Host crystal	$\tau_{\text{rad}}(^4\text{I}_{13/2}), \text{ ms}$	$\tau_{\text{rad}}(^4\text{I}_{11/2}), \text{ ms}$	$\beta_{\text{JF}}(^4\text{I}_{11/2} \rightarrow ^4\text{I}_{13/2}), \%$
CaF <sub>2</sub>	7.09	6.53	14.9
(Ca,Sr)F <sub>2</sub>	7.64	7.06	15.8
SrF <sub>2</sub>	7.57	6.99	16.0
(Sr,Ba)F <sub>2</sub>	7.90	7.56	16.5
BaF <sub>2</sub>	7.52	7.11	16.1

176

<sup>a</sup> $\tau_{\text{rad}}$  – radiative lifetime,  $\beta_{\text{JF}}$  – luminescence branching ratio.

177

### 4.3 Emission spectra and luminescence lifetimes

178

The luminescence spectra of Er<sup>3+</sup> ions in the mid-infrared (the <sup>4</sup>I<sub>11/2</sub> → <sup>4</sup>I<sub>13/2</sub> transition) were measured using an optical spectrum analyzer (OSA, Yokogawa AQ6376) and a ZrF<sub>4</sub> fiber. The excitation source was a Ti:Sapphire laser tuned to ~970 nm. The OSA was purged with N<sub>2</sub> gas. To remove the effect of the residual water vapor absorption in air, the set-up was calibrated using a 20 W quartz iodine lamp.

179

The stimulated-emission (SE) cross-sections,  $\sigma_{\text{SE}}$ , were calculated using the Füchtbauer-Ladenburg equation [39]:

180

$$\sigma_{\text{SE}}(\lambda) = \frac{\lambda^5}{8\pi \langle n \rangle^2 \tau_{\text{rad}} c} \frac{B(\text{JF})W(\lambda)}{\int \lambda W(\lambda) d\lambda}, \quad (1)$$

181

where  $\lambda$  is the light wavelength,  $\langle n \rangle$  is the refractive index of the crystal at the mean emission wavelength,  $\tau_{\text{rad}}$  corresponds to the <sup>4</sup>I<sub>11/2</sub> state and  $\beta_{\text{JF}}$  – to the <sup>4</sup>I<sub>11/2</sub> → <sup>4</sup>I<sub>13/2</sub> transition (cf. Table 3),  $c$  is the speed of light, and  $W(\lambda)$  is the measured luminescence spectrum corrected for the response of the set-up.

182

The SE cross-section spectra for Er<sup>3+</sup> ions in MF<sub>2</sub> crystals are shown in Fig. 5. Similarly to the absorption spectra, a profound inhomogeneous broadening is observed for both the parent and “mixed” Er<sup>3+</sup>:MF<sub>2</sub> crystals owing to the rare earth ion clustering. For all the studied crystals, the emission spectra are very broad extending from 2.55 to 3.05  $\mu\text{m}$  and the main emission peak appears around 2.72  $\mu\text{m}$ . Such a behavior is beneficial for broadly tunable and potentially

183

184

185

186

187

188

189

190

191

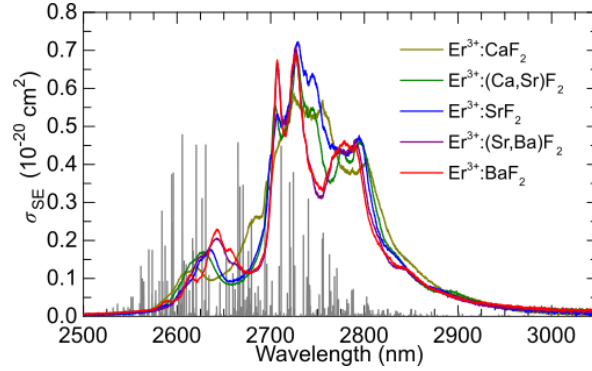
192

193

194



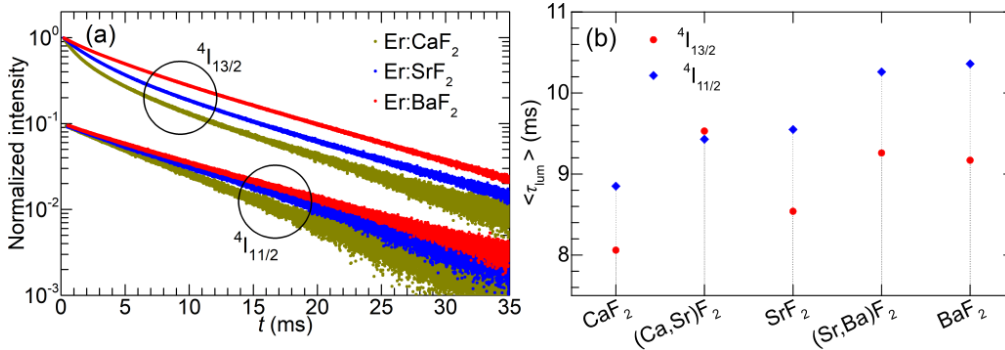
195 mode-locked lasers. The spectra become more structured in the  $M = \text{Ca} \rightarrow \text{Sr} \rightarrow \text{Ba}$  series.  
 196 Also for the solid-solution compounds, a great similarity between the emission spectra of  
 197  $(\text{Er}^{3+}:(\text{Ca},\text{Sr})\text{F}_2$  and  $\text{Er}^{3+}:\text{SrF}_2)$  and  $(\text{Er}^{3+}:(\text{Sr},\text{Ba})\text{F}_2$  and  $\text{Er}^{3+}:\text{BaF}_2)$  crystals is observed.



198  
 199 **Fig. 5.** Stimulated-emission (SE) cross-sections,  $\sigma_{\text{SE}}$ , for the  ${}^4\text{I}_{11/2} \rightarrow {}^4\text{I}_{13/2}$   $\text{Er}^{3+}$   
 200 transition in  $\text{MF}_2$  crystals, corrected for the structured water vapor absorption in air (in *grey*, arb. units, according  
 201 to the HITRAN database).

202 The highest SE cross-section is observed for  $\text{Er}^{3+}:\text{SrF}_2$ ,  $\sigma_{\text{SE}} = 7.19 \times 10^{-21} \text{ cm}^2$  at 2729 nm  
 203 and at longer wavelengths, two other intense and broad peaks appear ( $\sigma_{\text{SE}} = 6.38 \times 10^{-21} \text{ cm}^2$  at  
 204 2745 nm and  $4.69 \times 10^{-21} \text{ cm}^2$  at 2794 nm).

205 Luminescence decays were studied under resonant excitation using a ns optical parametric  
 206 oscillator (Horizon, Continuum), a 1/4 m monochromator (Oriel 77200), an InGaAs detector  
 207 and an 8 GHz oscilloscope (DSA70804B, Tektronix). To reduce the reabsorption (radiation  
 208 trapping) effect on the measured kinetics, the samples were finely ground into powders. The  
 209 measured luminescence decay curves from the  ${}^4\text{I}_{13/2}$  and  ${}^4\text{I}_{11/2}$   $\text{Er}^{3+}$  states in the three parent  
 210 crystals,  $\text{CaF}_2$ ,  $\text{SrF}_2$  and  $\text{BaF}_2$ , are shown in Fig. 6(a). They deviate from the single-exponential  
 211 law (especially for  ${}^4\text{I}_{13/2}$ ) owing to the strong ETU from these long-living states. Thus, the mean  
 212 luminescence lifetimes  $\langle \tau_{\text{lum}} \rangle = \int t \cdot I(t) dt / \int I(t) dt$  were determined.



213  
 214 **Fig. 6.** Luminescence dynamics from the  ${}^4\text{I}_{13/2}$  and  ${}^4\text{I}_{11/2}$   $\text{Er}^{3+}$  manifolds in  $\text{MF}_2$  crystals: (a)  
 215 luminescence decay curves under resonant excitation of  $\text{Er}^{3+}$  ions in  $\text{CaF}_2$ ,  $\text{SrF}_2$ , and  $\text{BaF}_2$ ,  $\lambda_{\text{exc}} =$   
 216  $1.48 \mu\text{m}$ ,  $\lambda_{\text{lum}} = 1.57 \mu\text{m}$  (the  ${}^4\text{I}_{13/2}$  state),  $\lambda_{\text{exc}} = 0.97 \mu\text{m}$ ,  $\lambda_{\text{lum}} = 1.01 \mu\text{m}$  (the  ${}^4\text{I}_{11/2}$  state); (b) mean  
 217 luminescence lifetimes  $\langle \tau_{\text{lum}} \rangle$  as a function of the host composition.

218 The summary of the  $\langle \tau_{\text{lum}} \rangle$  values for the five studied  $\text{Er}^{3+}:\text{MF}_2$  crystals is given in Fig. 6(b).  
 219 With increasing the average radius / atomic mass of the  $\text{M}^{2+}$  host-forming cations (in the  $M =$   
 220  $\text{Ca} \rightarrow \text{Sr} \rightarrow \text{Ba}$  series), and, accordingly, decreasing the phonon energy of the host matrix, both  
 221 the  ${}^4\text{I}_{13/2}$  and  ${}^4\text{I}_{11/2}$  luminescence lifetimes tend to increase, from 8.06 / 8.85 ms ( $\text{Er}^{3+}:\text{CaF}_2$ ) to  
 222 8.54 / 9.55 ms ( $\text{Er}^{3+}:\text{SrF}_2$ ) and further to 9.17 / 10.36 ms ( $\text{Er}^{3+}:\text{BaF}_2$ ). This behavior agrees with  
 223 that for the calculated radiative lifetimes of these manifolds. The ratio of the upper-to-lower



224 laser level lifetimes is favorable for all the studied crystals being weakly dependent on the host  
 225 matrix composition. The long luminescence lifetime of the upper laser level for the mid-infrared  
 226 transition ( ${}^4I_{11/2}$ ) is a prerequisite for a low-threshold behavior.

227 Note that the measured luminescence lifetimes are slightly exceeding the radiative ones  
 228 calculated using the J-O theory (cf. Table 3). One possible reason for that is the residual  
 229 reabsorption effect within the  $\text{Er}^{3+}$  ion clusters.

230

**Table 4. Spectroscopic Characteristics<sup>a</sup> of  $\text{Er}^{3+}:\text{MF}_2$  Crystals**

Parameter / Crystal	$\text{CaF}_2$	$(\text{Ca,Sr})\text{F}_2$	$\text{SrF}_2$	$(\text{Sr,Ba})\text{F}_2$	$\text{BaF}_2$
$\lambda_{\text{abs}}$ , nm	967.6	969.7	969.5	971.4	972.3
$\sigma_{\text{abs}}$ , $10^{-21}$ $\text{cm}^2$	2.22	2.91	2.59	3.04	2.77
$\lambda_{\text{em}}$ , nm	2724.8	2727.6	2728.9	2726.6	2726.5
$\sigma_{\text{SE}}$ , $10^{-21}$ $\text{cm}^2$	5.87	6.90	7.22	7.11	6.92
$\langle\tau_{\text{lum}}\rangle({}^4I_{13/2})$ , ms	8.06	9.53	8.54	9.26	9.17
$\langle\tau_{\text{lum}}\rangle({}^4I_{11/2})$ , ms	8.85	9.43	9.55	10.26	10.36

231

232

<sup>a</sup> $\lambda_{\text{abs}}$ ,  $\lambda_{\text{em}}$  – peak absorption / emission wavelengths, respectively,  $\sigma_{\text{abs}}$ ,  $\sigma_{\text{SE}}$  – peak absorption / SE cross-sections, respectively,  $\langle\tau_{\text{lum}}\rangle$  - average luminescence lifetime.

233

#### 4.4 Low-temperature spectroscopy

234

235

236

237

238

239

For low-temperature (LT, 12 K) absorption and luminescence studies, we have used an APD DE-202 closed-cycle cryo-cooler equipped with an APD HC 2 Helium vacuum cryo-compressor and a Laceshore 330 temperature controller. For absorption measurements, a 20 W quartz lamp with a calibrated spectral output was used. The spectra were measured using optical spectrum analyzers (Ando AQ6315A and Yokogawa AQ6375E). The luminescence was excited by a Ti:Sapphire laser tuned to  $\sim 800$  nm.

240

241

242

243

244

245

The LT absorption and emission spectra are shown in Fig. 7 and Fig. 8, respectively. In each graph, we compare the spectrum of a “mixed” compound with those of both parent crystals. The LT absorption spectra were plotted versus the phonon energy giving access to the splitting of the  ${}^4I_{13/2}$  and  ${}^4I_{11/2}$  excited-states, while the LT emission spectra were plotted versus ( $E_{\text{ZPL}} - \text{photon energy}$ ), where  $E_{\text{ZPL}}$  is the zero-phonon line (ZPL) energy giving access to the splitting of the ground-state  ${}^4I_{15/2}$ .

246

247

248

249

250

251

252

253

254

255

256

By analyzing the spectra, several conclusions can be derived:

257

258

259

260

261

262

263

264

265

266

267

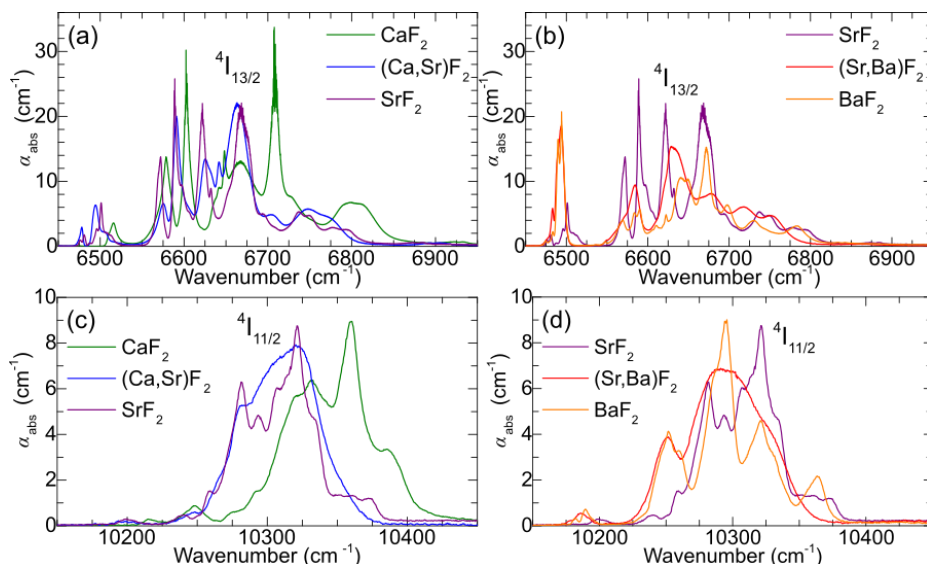
(i) The absorption and emission spectra of  $\text{Er}^{3+}$  ions in  $\text{MF}_2$  crystals contain very broad bands even at 12 K indicating a significant inhomogeneous spectral broadening due to the rare-earth ion clustering. The spectra become more structured in the series  $\text{M} = \text{Ca} \rightarrow \text{Sr} \rightarrow \text{Ba}$  indicating smaller variety of cluster geometries;

(ii) The spectra of “mixed” fluorite-type crystals exhibit additional broadening as compared to the corresponding parent compounds due to the presence of two different host-forming cations. The spectra of such “mixed” crystals are more similar to those of the heavier-cation parent (e.g.,  $(\text{Ca,Sr})\text{F}_2$  and  $\text{SrF}_2$ ,  $(\text{Ba,Sr})\text{F}_2$  and  $\text{BaF}_2$ ). This corroborates the observation made in Section 4.3, confirming that the majority of  $\text{Er}^{3+}$  ions tend to reside in the vicinity of heavier cations within “mixed” crystals;

(iii) The total Stark splitting of  $\text{Er}^{3+}$  multiplets in clusters in  $\text{MF}_2$  crystals decreases in the  $\text{M} = \text{Ca} \rightarrow \text{Sr} \rightarrow \text{Ba}$  series, and the corresponding barycenter energies experience a progressive red-shift. The strength of the crystal-field is expected to be larger for smaller sites (shorter  $\text{M} - \text{F}$  and  $\text{M} - \text{M}$  distances, in our case) due to the stronger lattice distortion on the dopant ion. Indeed, the lattice constant increases in the series  $\text{CaF}_2$  (5.45 Å)  $\rightarrow$   $\text{SrF}_2$  (5.80 Å)  $\rightarrow$   $\text{BaF}_2$  (6.20 Å).

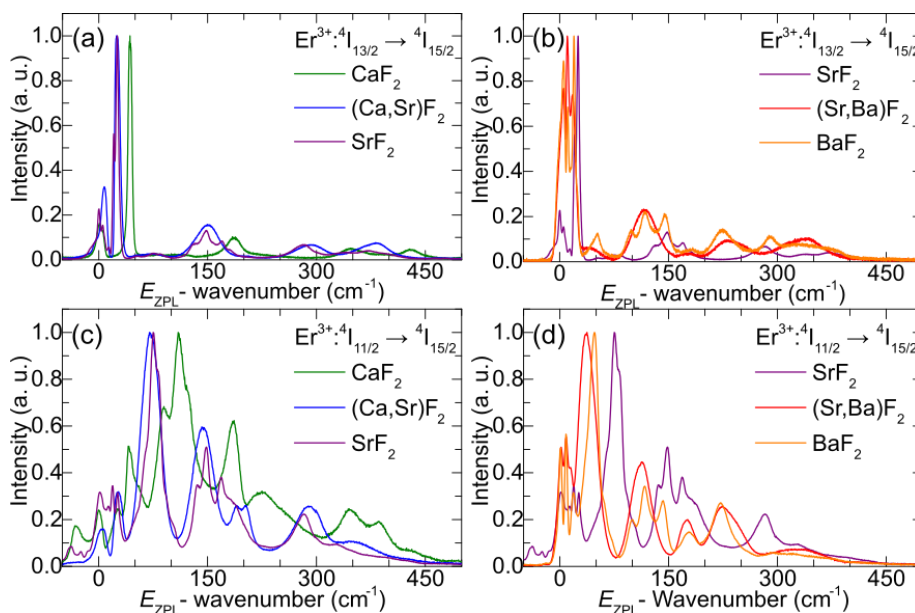
Based on the LT absorption and emission spectra, the crystal-field splitting of the  ${}^4I_{15/2}$ ,  ${}^4I_{13/2}$  and  ${}^4I_{11/2}$  multiplets of  $\text{Er}^{3+}$  ions forming clusters in the three parent  $\text{MF}_2$  crystals ( $\text{M} = \text{Ca}, \text{Sr}, \text{Ba}$ ), was determined, Table 5. The experimental Stark splitting of the  ${}^4I_{11/2}$  and  ${}^4I_{13/2}$  multiplets relevant for the 2.8  $\mu\text{m}$  laser operation is also compared in Fig. 9. In the previous studies on site-selective spectroscopy of  $\text{Er}^{3+}$  ions in  $\text{CaF}_2$  crystals grown under oxygen-free atmosphere, multiple possible sites were identified [40-42]. At very low doping levels ( $<0.05$  at.%), the  $\text{Er}^{3+}$

268 ions are mostly isolated and are distributed over tetragonal (A,  $C_{4v}$ ), trigonal (B,  $C_{3v}$ ) and cubic  
 269 ( $O_h$ ) sites, depending on the relative position of the charge-compensating interstitial fluorine anion  
 270 ( $F_i^-$ ), namely at the (1,0,0) positions, at the (1,1,1) positions or sufficiently far from the dopant ion  
 271 to exert negligible perturbation, respectively [40]. For higher doping levels of  $>0.1$  at.%, the  
 272 dopant ions form clusters of several types (assigned as C-sites, being close to dimers with a  
 273 distorted  $C_{3v}$  symmetry, and D(1) and D(2) sites corresponding to larger agglomerates of  $Er^{3+}$  -  
 274  $F_i^-$  pairs).



275  
 276  
 277

**Fig. 7.** (a-d) LT (12 K) absorption spectra of  $Er^{3+}$  ions in fluorite-type crystals: (a,b) the  ${}^4I_{15/2} \rightarrow {}^4I_{13/2}$  transition; (c,d)  ${}^4I_{15/2} \rightarrow {}^4I_{11/2}$  transition.  $\alpha_{abs}$  – absorption coefficient.



278  
 279  
 280

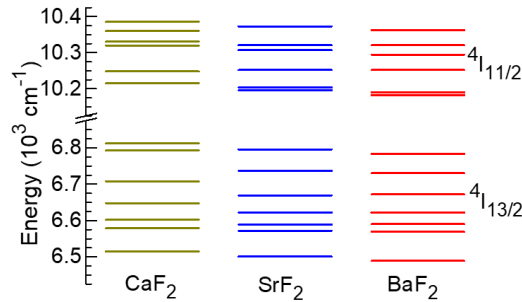
**Fig. 8.** (a-d) LT (12 K) luminescence spectra of  $Er^{3+}$  ions in fluorite-type crystals: (a,b) the  ${}^4I_{13/2} \rightarrow {}^4I_{15/2}$  transition; (c,d)  ${}^4I_{11/2} \rightarrow {}^4I_{15/2}$  transition.  $E_{ZPL}$  – zero-phonon-line energy.

281 For the studied heavily doped  $\text{Er}^{3+}:\text{MF}_2$  crystals, we were not able to confirm the existence of  
 282 two significantly different groups of ion clusters (D(1) and D(2)), as the LT emission spectra were  
 283 almost independent on the excitation wavelength. Moreover, the bands in the LT spectra of  $\sim 5$   
 284 at.%  $\text{Er}^{3+}$ -doped crystals (assigned to a single type of cluster D sites) experience an additional  
 285 broadening and spectral shifts as compared to those in 0.1 at.%  $\text{Er}^{3+}$ -doped crystals (assigned to  
 286 D(1) and D(2) sites). Thus, we assumed that almost all the  $\text{Er}^{3+}$  ions form large-scale agglomerates  
 287 (D) with relatively close spectroscopic properties. Previously, it was suggested that for all the  
 288 heavily doped  $\text{MF}_2$  crystals ( $M = \text{Ca}, \text{Sr}, \text{Ba}$ ) and their solid-solutions, such agglomerates most  
 289 likely correspond to hexameric  $\text{Y}_6\text{F}_{37}$  superstructure units, which are nearly identical in volume  
 290 and shape to the  $\text{Ca}_2\text{F}_{32}$  building blocks of the fluorite lattice and, consequently, they can be  
 291 easily incorporated into this lattice while accommodating the excess  $\text{F}_i^-$  anions [5,43]. The local  
 292 crystal-field symmetry for the dopant ions in  $\text{Y}_6\text{F}_{37}$  clusters is tetragonal ( $C_{4v}$ ) [5].

293

**Table 5. Crystal-Field Splitting of Selected  $\text{Er}^{3+}$  Multiplets in  $\text{CaF}_2$ ,  $\text{SrF}_2$ , and  $\text{BaF}_2$**

Crystal	$\text{Er}^{3+}$ $^{2S+1}L_J$	Sub-level / Energy ( $\text{cm}^{-1}$ )							
		1	2	3	4	5	6	7	8
$\text{CaF}_2$	$^4I_{15/2}$	0	42	90	110	186	228	346	387
	$^4I_{13/2}$	6516	6579	6602	6648	6708	6793	6812	
	$^4I_{11/2}$	10215	10248	10320	10331	10360	10386		
$\text{SrF}_2$	$^4I_{15/2}$	0	25	63	75	148	187	283	330
	$^4I_{13/2}$	6501	6572	6589	6622	6669	6737	6796	
	$^4I_{11/2}$	10196	10204	10282	10307	10321	10373		
$\text{BaF}_2$	$^4I_{15/2}$	0	18	34	48	117	142	222	293
	$^4I_{13/2}$	6489	6569	6590	6622	6672	6730	6784	
	$^4I_{11/2}$	10182	10190	10252	10295	10321	10363		



294

**Fig. 9.** Experimental Stark splitting of the  $^4I_{11/2}$  and  $^4I_{13/2}$  multiplets of  $\text{Er}^{3+}$  ions forming clusters in heavily doped  $\text{Er}^{3+}:\text{MF}_2$  crystals.

295

296

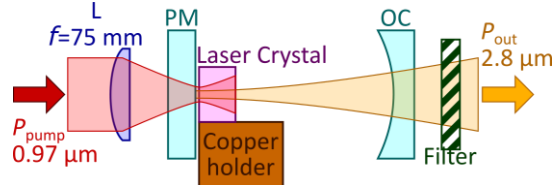
297 The analysis of Table 2 confirms a decreased total Stark splitting of the multiplets and a red-  
 298 shift of the zero-phonon line for  $\text{Er}^{3+}$  ions in the  $M = \text{Ca} \rightarrow \text{Sr} \rightarrow \text{Ba}$  series.

## 299 5. Laser operation

### 300 5.1 Laser setup

301 The scheme of the laser set-up is shown in Fig. 10. Cylindrical samples with a thickness of 6.53-  
 302 6.99 mm and a diameter of  $\sim 7$  mm were cut from the central parts of the as-grown  $\text{Er}^{3+}:\text{MF}_2$   
 303 crystal boules. They were polished to laser-grade quality with good parallelism ( $< 5^\circ$ ) from both  
 304 sides and left uncoated. The laser elements were mounted on a passively cooled Cu-holder using  
 305 a silver paint for better heat removal. A hemispherical cavity was implemented. It was formed by  
 306 a flat pump mirror (PM) coated for high transmission (HT,  $T = 85.7\%$ ) at  $0.97 \mu\text{m}$  and high  
 307 reflection (HR) at  $2.6 - 3.0 \mu\text{m}$ , and a set of concave (radius of curvature:  $\text{RoC} = -100 \text{ mm}$ )  
 308 output couplers (OC) having a transmission  $T_{\text{OC}}$  in the range of 0.33% - 4% at  $2.7 - 2.9 \mu\text{m}$ .  
 309 The crystal was placed near the PM at a small distance ( $< 1 \text{ mm}$ ). The geometrical cavity length  
 310 was  $\sim 99 \text{ mm}$ . The pump source was a CW Ti:Sapphire laser delivering up to 3.2 W at  $0.97 \mu\text{m}$

311 (addressing the  ${}^4I_{15/2} \rightarrow {}^4I_{11/2}$   $\text{Er}^{3+}$  absorption peak) with a diffraction-limited beam quality ( $M^2$   
 312  $\approx 1$ ). The pump radiation was focused into the laser crystal through the PM using an  
 313 antireflection-coated achromatic lens (focal length:  $f = 75$  mm) resulting in a pump spot size of  
 314  $2w_p = 66 \pm 5$   $\mu\text{m}$ . The pumping was in single pass. The residual (non-absorbed) pump after the  
 315 OC was filtered out using a long-pass filter (Spectrogon, LP1400). The laser spectra were  
 316 measured using a  $\text{ZrF}_4$  fiber (Thorlabs) and a spectrum analyzer (Bristol, 771 series). The laser  
 317 mode profile in the far-field was captured using a camera (Pyrocam IIIHR, Ophir-Spiricon).

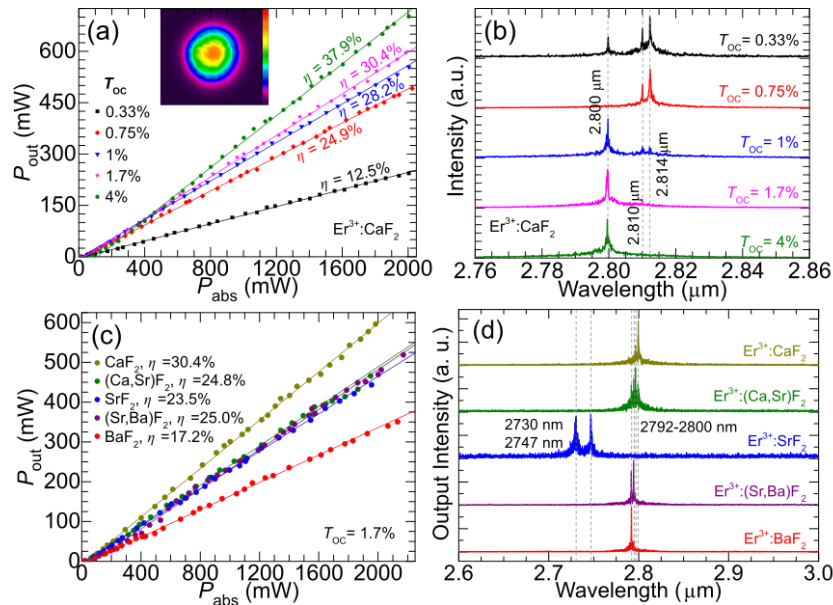


318  
 319  
 320

**Fig. 10.** Schematic of the laser setup: L – aspherical focusing lens; PM – flat pump mirror; OC – curved output coupler.

### 321 5.2 Laser performance

322 CW mid-infrared laser operation was obtained with all five studied  $\text{Er}^{3+}:\text{MF}_2$  crystals. The best  
 323 laser performance was achieved with the  $\text{Er}^{3+}:\text{CaF}_2$  crystal: an output power of 702 mW was  
 324 extracted at 2800 nm with a slope efficiency  $\eta$  of 37.9% (vs. the absorbed pump power) when  
 325 using the output coupler with  $T_{\text{OC}} = 4\%$ , Fig. 11(a). With increasing output coupling from 0.33%  
 326 to 4%, the laser threshold gradually increased from 16 mW to 60 mW. For  $\text{Er}^{3+}:\text{CaF}_2$ , the  
 327 measured pump absorption reached 81.9%. The optical-to-optical efficiency (vs. the pump power  
 328 incident on the crystal)  $\eta_{\text{opt}}$  was 31.0%. The output dependences were linear within the studied  
 329 range of pump powers. Further power scaling was limited by the available pump. The achieved  
 330 laser slope efficiency is slightly higher than the Stokes limit,  $\eta_{\text{St,L}} = \lambda_p/\lambda_L = 34.6\%$ , indicating the  
 331 role of the ETU process  ${}^4I_{13/2} + {}^4I_{13/2} \rightarrow {}^4I_{9/2} + {}^4I_{15/2}$ , cf. Fig. 1, refilling the upper laser level and  
 332 depopulating the intermediate  ${}^4I_{13/2}$  state.



333  
 334  
 335  
 336  
 337

**Fig. 11.** Mid-infrared  $\text{Er}^{3+}:\text{MF}_2$  lasers: (a,b)  $\text{Er}^{3+}:\text{CaF}_2$  laser: (a) input-output dependences,  $\eta$  – slope efficiency, *inset* – far-field mode profile,  $P_{\text{abs}} \sim 1.5$  W,  $T_{\text{OC}} = 1.7\%$ ; (b) typical laser spectra; (c,d) a comparison of (c) power transfer characteristics and (d) laser spectra for five  $\text{Er}^{3+}:\text{MF}_2$  crystals,  $T_{\text{OC}} = 1.7\%$ .

338 The typical emission spectra of the  $\text{Er}^{3+}:\text{CaF}_2$  laser are shown in Fig. 11(b), measured well  
 339 above the laser threshold. For small output coupling (<1%), laser emission at 2810 and 2814 nm  
 340 was observed and for higher  $T_{\text{OC}}$ , the laser operated at 2800 nm. These wavelengths correspond  
 341 to the long-wave emission peak of  $\text{Er}^{3+}$  ions in  $\text{CaF}_2$  and match the transparency ranges between  
 342 the structured water vapor absorption lines (cf. Fig. 5). Note that due to strong resonant excited-  
 343 state absorption from the terminal laser level with a non-negligible population,  ${}^4\text{I}_{13/2} \rightarrow {}^4\text{I}_{11/2}$ ,  
 344 causing reabsorption of the laser photons, the  ${}^4\text{I}_{11/2} \rightarrow {}^4\text{I}_{13/2}$   $\text{Er}^{3+}$  laser transition represents a  
 345 quasi-three-level laser scheme with reabsorption, which explains the blue-shift of the laser  
 346 spectra with increasing the output coupling.

347 The  $\text{Er}^{3+}:\text{CaF}_2$  laser operated on the fundamental transverse mode, as confirmed by the  
 348 measured  $M^2 < 1.1$ , and the beam profile in the far-field was nearly circular, see the inset in  
 349 Fig. 11(a).

350 The output performance and laser spectra of five  $\text{Er}^{3+}:\text{MF}_2$  crystals are directly compared in  
 351 Fig. 11(c,d) using the same output coupling ( $T_{\text{OC}} = 1.7\%$ ). The slope efficiency gradually  
 352 decreased in the sequence  $\text{Er}^{3+}:\text{CaF}_2 \rightarrow \text{Er}^{3+}:\text{SrF}_2$  and Sr-containing crystals  $\rightarrow \text{Er}^{3+}:\text{BaF}_2$ , while  
 353 the laser threshold was in the range of 17 – 28 mW for all the crystals, being only slightly higher  
 354 for Ba-containing ones. The laser emission occurred at 2792 – 2800 nm, except of  $\text{Er}^{3+}:\text{SrF}_2$  for  
 355 which the laser operated at shorter wavelengths, 2730 and 2747 nm. The output characteristics  
 356 of mid-infrared  $\text{Er}^{3+}:\text{MF}_2$  lasers are summarized in Table 6. More details about the 2.8  $\mu\text{m}$  laser  
 357 performance of Ba-containing crystals can be found in [44].

358

**Table 6. Output Characteristics<sup>a</sup> of Mid-Infrared  $\text{Er}^{3+}:\text{MF}_2$  Lasers ( $T_{\text{OC}} = 1.7\%$ )**

Parameter / Crystal	$\text{CaF}_2$	$(\text{Ca,Sr})\text{F}_2$	$\text{SrF}_2$	$(\text{Sr,Ba})\text{F}_2$	$\text{BaF}_2$
$t$ , mm	6.81	6.99	6.53	6.99	6.66
$\lambda_p$ , nm	967.8	969.7	969.5	971.4	971.2
$\eta_{\text{abs}}$ , %	81.9	84.3	76.1	83.3	83.8
$P_{\text{out}}$ , mW	596	466	443	519	350
$\lambda_L$ , nm	2800	2796	2747	2794	2792
$P_{\text{th}}$ , mW	20	17	20	28	26
$\eta$ , %	30.4	24.8	23.5	25.0	17.2

359

<sup>a</sup> $t$  – crystal thickness,  $\lambda_p$  – pump wavelength,  $\eta_{\text{abs}}$  – pump absorption under lasing conditions,

360

$P_{\text{out}}$  – output power,  $\lambda_L$  – laser wavelength,  $P_{\text{th}}$  – laser threshold,  $\eta$  – slope efficiency.

361

## 6. Conclusions

362

Fluorite-type  $\text{Er}^{3+}:\text{MF}_2$  parent and solid-solution crystals feature low-phonon-energy behavior,  
 363 very broad absorption and mid-infrared emission spectral bands, owing to the profound  $\text{Er}^{3+}$  ion  
 364 clustering and long  ${}^4\text{I}_{11/2}$  and  ${}^4\text{I}_{13/2}$  luminescence lifetimes. As for the “mixed” compounds, their  
 365 advantage is the lower melting points with respect to the corresponding parents. Considering the  
 366 high thermal conductivity of these materials, the  $\text{Er}^{3+}:\text{MF}_2$  crystals are very promising for the  
 367 development of power-scalable and broadly tunable low-threshold mid-infrared lasers emitting at  
 368  $\sim 2.8 \mu\text{m}$ . Based on a detailed comparative spectroscopic study of five 5 at.%  $\text{Er}^{3+}:\text{MF}_2$  fluorite-  
 369 type crystals, including the parent compounds  $\text{CaF}_2$ ,  $\text{SrF}_2$ ,  $\text{BaF}_2$ , and “mixed” ones,  $(\text{Ca,Sr})\text{F}_2$   
 370 and  $(\text{Sr,Ba})\text{F}_2$ , the following conclusions are derived:

371

(i) The phonon energy of  $\text{Er}^{3+}:\text{MF}_2$  crystals monotonously decreases with the square root of  
 372 the  $M^{2+}$  cationic mass, from  $321 \text{ cm}^{-1}$  ( $\text{Er}^{3+}:\text{CaF}_2$ ) to  $242 \text{ cm}^{-1}$  ( $\text{Er}^{3+}:\text{BaF}_2$ ). Such a low-phonon  
 373 energy behavior is a prerequisite for almost vanishing multiphonon non-radiative path from  
 374 both the  ${}^4\text{I}_{11/2}$  and  ${}^4\text{I}_{13/2}$   $\text{Er}^{3+}$  manifolds, as confirmed by the luminescence decay studies and the  
 375 Judd-Ofelt analysis yielding the radiative lifetimes;

376

(ii) In the  $M = \text{Ca} \rightarrow \text{Sr} \rightarrow \text{Ba}$  series, the absorption and mid-infrared emission spectra  
 377 gradually become narrower and more structured, which is linked to the decreasing complexity  
 378 of  $\text{Er}^{3+}$  clusters, and the luminescence lifetimes of the  ${}^4\text{I}_{13/2} / {}^4\text{I}_{11/2}$   $\text{Er}^{3+}$  manifolds increase, from  
 379 8.06 / 8.85 ms ( $\text{Er}^{3+}:\text{CaF}_2$ ) to 9.17 / 10.36 ms ( $\text{Er}^{3+}:\text{BaF}_2$ ) because of a decrease in the crystal

380 field strength. The observed ratio of the upper-to-lower laser level lifetimes and their values are  
381 favorable for low-threshold mid-infrared laser operation;

382 (iii) The  $\text{Er}^{3+}$  ions in “mixed” crystals tend to reside in a local environment predominantly  
383 composed of the larger / heavier  $\text{M}^{2+}$  cations, leading to a great similarity between the spectra  
384 of  $\text{Er}^{3+}:\text{SrF}_2$  and  $\text{Er}^{3+}:(\text{Ca},\text{Sr})\text{F}_2$ ,  $\text{Er}^{3+}:\text{BaF}_2$  and  $\text{Er}^{3+}:(\text{Sr},\text{Ba})\text{F}_2$ . At LT, the spectra of  $\text{Er}^{3+}$  ions  
385 in solid-solution crystals exhibit a notable inhomogeneous broadening;

386 (iv) For the doping level of 5 at.%  $\text{Er}^{3+}$  in  $\text{MF}_2$  crystals, the LT spectroscopy reveals the  
387 existence of a single class of  $\text{Er}^{3+}$  clusters with rather close absorption / emission properties (D  
388 centers), contrary to crystals with low doping levels subject to ion clustering of various nature  
389 (D(1) and D(2)).

390 In the present work, we employed high-brightness pumping to reveal the potential of  
391  $\text{Er}^{3+}:\text{MF}_2$  crystals for efficient lasing at  $\sim 2.8 \mu\text{m}$ . Further power scaling is envisioned by using  
392 powerful InGaAs laser diodes as pump sources which is feasible owing to the good thermal  
393 properties of these compounds. Further improvement of the slope efficiency, especially for Sr  
394 and Ba-containing crystals should involve an optimization of the  $\text{Er}^{3+}$  doping level for boosting  
395 the ETU efficiency. One hypothesis here is that a reduction in the cluster complexity may lead  
396 to weaker energy-transfer processes. Another idea is the  $\text{Er}^{3+},\text{Pr}^{3+}$  codoping for quenching the  
397 metastable  $\text{Er}^{3+}$  lower-laser level ( ${}^4\text{I}_{13/2}$ ).

398 **Funding.** French Agence Nationale de la Recherche (ANR) SPLENDID2 (ANR-19-CE08-0028). “RELANCE”  
399 Chair of Excellence project funded by the Normandy Region.

400 **Disclosures.** The authors declare no conflicts of interest.

401 **Data availability.** Data underlying the results presented in this paper are not publicly available at this time but may  
402 be obtained from the authors upon reasonable request.

## 403 References

- 404 1. C. Labbe, J. L. Doualan, P. Camy, R. Moncorgé, and M. Thuau, “The 2.8  $\mu\text{m}$  laser properties of  $\text{Er}^{3+}$  doped  
405  $\text{CaF}_2$  crystals,” *Opt. Commun.* **209**(1-3), 193-199 (2002).
- 406 2. F. Druon, S. Ricaud, D. N. Papadopoulos, A. Pellegrina, P. Camy, J. L. Doualan, R. Moncorgé, A. Courjaud, E.  
407 Mottay and P. Georges, “On  $\text{Yb}:\text{CaF}_2$  and  $\text{Yb}:\text{SrF}_2$ : review of spectroscopic and thermal properties and their  
408 impact on femtosecond and high power laser performance,” *Opt. Mater. Express* **1**(3), 489-502 (2011).
- 409 3. P. Camy, J. L. Doualan, S. Renard, A. Braud, V. Ménard, and R. Moncorgé, “ $\text{Tm}^{3+}:\text{CaF}_2$  for 1.9  $\mu\text{m}$  laser  
410 operation,” *Opt. Commun.* **236**(4-6), 395-402 (2004).
- 411 4. V. Petit, P. Camy, J.-L. Doualan, X. Portier, and R. Moncorgé, “Spectroscopy of  $\text{Yb}^{3+}:\text{CaF}_2$ : from isolated  
412 centers to clusters,” *Phys. Rev. B* **78**(8), 085131-1-12 (2008).
- 413 5. S. A. Kazanskii, and A. I. Ryskin, “Group-III Ion Clusters in Activated Fluorite-Like Crystals,” *Phys. Solid  
414 State* **44**(8), 1415-1425 (2002).
- 415 6. B. Lacroix, C. Genevois, J. L. Doualan, G. Brasse, A. Braud, P. Ruterana, P. Camy, E. Talbot, R. Moncorgé,  
416 and J. Margerie, “Direct imaging of rare-earth ion clusters in  $\text{Yb}:\text{CaF}_2$ ,” *Phys. Rev. B* **90**(12), 125124-1-14  
417 (2014).
- 418 7. V. Petit, J. L. Doualan, P. Camy, V. Ménard and R. Moncorgé, “CW and tunable laser operation of  $\text{Yb}^{3+}$  doped  
419  $\text{CaF}_2$ ,” *Appl. Phys. B* **78**(6), 681-684 (2004).
- 420 8. R. Thouroude, A. Tyazhev, A. Hideur, P. Loiko, P. Camy, J. L. Doualan, H. Gilles, and M. Laroche, “Widely  
421 tunable in-band-pumped  $\text{Tm}:\text{CaF}_2$  laser,” *Opt. Lett.* **45**(16), 4511-4514 (2020).
- 422 9. G. Machinet, P. Sevillano, F. Guichard, R. Dubrasquet, P. Camy, J. L. Doualan, R. Moncorgé, P. Georges, F.  
423 Druon, D. Descamps and E. Cormier, “High-brightness fiber laser-pumped 68 fs-2.3 W Kerr-lens mode-locked  
424  $\text{Yb}:\text{CaF}_2$  oscillator,” *Opt. Lett.* **38**(9), 4008-4010 (2013).
- 425 10. A. Lucca, G. Debourg, M. Jacquemet, F. Druon, F. Balembos, P. Georges, P. Camy, J. L. Doualan and R.  
426 Moncorgé, “High-power diode-pumped  $\text{Yb}^{3+}:\text{CaF}_2$  femtosecond laser,” *Opt. Lett.* **29**(23), 2767-2769 (2004).
- 427 11. P. Loiko, A. Braud, L. Guillemot, J.L. Doualan, A. Benayad, and P. Camy, “Cross-relaxation and ion clustering  
428 in  $\text{Tm}^{3+}:\text{CaF}_2$  crystals,” *Proc. SPIE* **11357**, 113570N (2020).
- 429 12. P. Camy, J. L. Doualan, A. Benayad, M. Von Edlinger, V. Ménard and R. Moncorgé, “Comparative  
430 spectroscopic and laser properties of  $\text{Yb}^{3+}$ -doped  $\text{CaF}_2$ ,  $\text{SrF}_2$  and  $\text{BaF}_2$  single crystals,” *Appl. Phys. B* **89**(4),  
431 539-542 (2007).
- 432 13. S. Bordj, H. Satha, A. Barros, D. Zambon, J. P. Jouart, M. Diaf, M., and R. Mahiou, “Spectroscopic  
433 characterization by up conversion of  $\text{Ho}^{3+}/\text{Yb}^{3+}$  codoped  $\text{CdF}_2$  single crystal” *Opt.Mater.* **118**, 111249 (2021).
- 434 14. M. Zhou, P. Zhang, X. Niu, J. Liao, Q. Chen, S. Zhu, Y. Hang, Q. Yang, H. Yin, Z. Li, and Z. Chen, “Ultra-  
435 broadband and enhanced near-infrared emission in Bi/Er co-doped  $\text{PbF}_2$  laser crystal,” *J. Alloys Compd.* **895**,  
436 162704 (2022).

- 437  
438  
439  
440  
441  
442  
443  
444  
445  
446  
447  
448  
449  
450  
451  
452  
453  
454  
455  
456  
457  
458  
459  
460  
461  
462  
463  
464  
465  
466  
467  
468  
469  
470  
471  
472  
473  
474  
475  
476  
477  
478  
479  
480  
481  
482  
483  
484  
485  
486  
487  
488  
489  
490  
491  
492  
493  
494  
495
15. W. Z. Xue, Z. L. Lin, H. J. Zeng, G. Zhang, P. Loiko, L. Basyrova, A. Benayad, P. Camy, V. Petrov, X. Mateos, L. Wang, and W. Chen, "Diode-pumped mode-locked Yb:BaF<sub>2</sub> laser," *Opt. Express* **30**(9), 15807-15818 (2022).
  16. S. V. Kuznetsov, V. A. Konyushkin, A. N. Nakladov, E. V. Chernova, P. A. Popov, A. A. Pynenkov, K. N. Nishchev, and P. P. Fedorov, "Thermophysical properties of single crystals of CaF<sub>2</sub>-SrF<sub>2</sub>-RF<sub>3</sub> (R= Ho, Pr) fluorite solid solutions," *Inorg. Mater.* **56**(9), 975-981 (2020).
  17. P. P. Fedorov, I. I. Buchinskaya, N. A. Ivanovskaya, V. V. Konvalova, S. V. Lavrishchev, and B. P. Sobolev, "CaF<sub>2</sub>-BaF<sub>2</sub> phase diagram," *Dokl. Phys. Chem.* **401**(4), 53-55. Nauka/Interperiodica (2025).
  18. P. A. Popov, A. A. Krugovoykh, V. A. Konyushkin, A. N. Nakladov, S. V. Kuznetsov, and P. P. Fedorov, "Thermal Conductivity of Sr<sub>1-x</sub>Ba<sub>x</sub>F<sub>2</sub> Single Crystals," *Inorg. Mater.* **57**(6), 629-633 (2021).
  19. D. Klimm, M. Rabe, R. Bertram, R. Uecker, and L. Parthier, "Phase diagram analysis and crystal growth of solid solutions Ca<sub>1-x</sub>Sr<sub>x</sub>F<sub>2</sub>," *J. Cryst. Growth* **310**(1), 152-155 (2008).
  20. R. H. Nafziger, "High-Temperature Phase Relations in the System BaF<sub>2</sub>-SrF<sub>2</sub>," *J. Am. Ceram. Soc.* **54**(9), 467-467 (1971).
  21. J. L. Doualan, P. Camy, A. Benayad, V. Ménard, R. Moncorgé, J. Boudeile, F. Druon, F. Balembois, and P. Georges, "Yb<sup>3+</sup> doped (Ca,Sr,Ba)F<sub>2</sub> for high power laser applications," *Laser Phys.* **20**(2), 533-536 (2010).
  22. K. Veselský, J. Šulc, H. Jelínková, M. E. Doroshenko, V. A. Konyushkin, and A. N. Nakladov, "Spectroscopic and laser properties of a broadly tunable diode-pumped Tm<sup>3+</sup>:CaF<sub>2</sub>-SrF<sub>2</sub> laser," *Laser Phys. Lett.* **17**(2), p.025802 (2020).
  23. J. Liu, X. Feng, X. Fan, Z. Zhang, B. Zhang, J. Liu, and L. Su, "Efficient continuous-wave and passive Q-switched mode-locked Er<sup>3+</sup>:CaF<sub>2</sub>-SrF<sub>2</sub> lasers in the mid-infrared region," *Opt. Lett.* **43**(10), 2418-2421 (2018).
  24. B. J. Dinerman and P. F. Moulton, "3- $\mu$ m cw laser operations in erbium-doped YSGG, GGG, and YAG," *Opt. Lett.* **19**(15), 1143-1145 (1994).
  25. G. A. Newburgh, and M. Dubinskii, "Power and efficiency scaling of Er:ZBLAN fiber laser," *Laser Phys. Lett.* **18**(9), 095102-1-6 (2021).
  26. L. Basyrova, P. Loiko, J. L. Doualan, A. Benayad, A. Braud, B. Viana, and P. Camy, "Thermal lensing, heat loading and power scaling of mid-infrared Er:CaF<sub>2</sub> lasers," *Opt. Express* **30**(5), 8092-8103 (2022).
  27. M. Zong, Y. Wang, Z. Zhang, J. Liu, L. Zhao, J. Liu, and L. Su, "High-power 2.8  $\mu$ m lasing in a lightly-doped Er: CaF<sub>2</sub> crystal," *J. Lumin.* **250**, 119089 (2022).
  28. R. Švejkar, J. Šulc, H. Jelínková, V. Kubeček, W. Ma, D. Jiang, Q. Wu, and L. Su, "Diode-pumped Er:SrF<sub>2</sub> laser tunable at 2.7  $\mu$ m," *Opt. Mater. Express* **8**(4), 1025-1030 (2018).
  29. J. Šulc, M. Němec, R. Švejkar, H. Jelínková, M. E. Doroshenko, P. P. Fedorov, and V. V. Osiko, "Diode-pumped Er:CaF<sub>2</sub> ceramic 2.7  $\mu$ m tunable laser," *Opt. Lett.* **38**(17), 3406-3409 (2013).
  30. J. P. Russell, "The Raman spectrum of calcium fluoride," *Proc. Phys. Soc.* (1958-1967), **85**(1), p.194 (1965).
  31. L. Su, J. Xu, W. Yang, X. Jiang, and Y. Dong, "Raman spectra of undoped and uranium doped CaF<sub>2</sub> single crystals," *Chin. Opt. Lett.* **3**(4), 219-221 (2005).
  32. R. K. Chang, B. Lacina, and P. S. Pershan, "Raman scattering from mixed crystals (Ca<sub>x</sub>Sr<sub>1-x</sub>)F<sub>2</sub> and (Sr<sub>x</sub>Ba<sub>1-x</sub>)F<sub>2</sub>," *Phys. Rev. Lett.* **17**(14), 755 (1966).
  33. A. Ubaldini, and M. M. Carnasciali, "Raman characterisation of powder of cubic RE<sub>2</sub>O<sub>3</sub> (RE= Nd, Gd, Dy, Tm, and Lu), Sc<sub>2</sub>O<sub>3</sub> and Y<sub>2</sub>O<sub>3</sub>," *J. Alloys Compd.* **454**(1-2), 374-378 (2008).
  34. W. T. Carnall, P. R. Fields, and K. Rajnak, "Electronic energy levels in the trivalent lanthanide aquo ions. I. Pr<sup>3+</sup>, Nd<sup>3+</sup>, Pm<sup>3+</sup>, Sm<sup>3+</sup>, Dy<sup>3+</sup>, Ho<sup>3+</sup>, Er<sup>3+</sup>, and Tm<sup>3+</sup>," *J. Chem. Phys.* **49**(10), 4424-4442 (1968).
  35. S. Normani, "Nd,Lu:CaF<sub>2</sub> for high-energy lasers" (Doctoral dissertation, Normandie Université) (2017).
  36. B. R. Judd, "Optical Absorption Intensities of Rare-Earth Ions," *Phys. Rev.* **127**(3), 750-761 (1962).
  37. G. S. Ofelt, "Intensities of Crystal Spectra of Rare-Earth Ions," *J. Chem. Phys.* **37**(3), 511-520 (1962).
  38. P. A. Tanner, V. R. K. Kumar, C. K. Jayasankar, and M. F. Reid, "Analysis of spectral data and comparative energy level parametrizations for Ln<sup>3+</sup> in cubic elpasolite crystals," *J. Alloys Compd.* **215**(1-2), 349-370 (1994).
  39. B. Aull, and H. Jenssen, "Vibronic interactions in Nd:YAG resulting in nonreciprocity of absorption and stimulated emission cross sections," *IEEE J. Quantum Electron.* **18**, 925-930 (1982).
  40. J. B. Fenn Jr, J. C. Wright, and F. K. Fong, "Optical study of ion-defect clustering in CaF<sub>2</sub>: Er<sup>3+</sup>," *J. Chem. Phys.* **59**(10), 5591-5599 (1973).
  41. D. R. Tallant, and J. C. Wright, "Selective laser excitation of charge compensated sites in CaF<sub>2</sub>: Er<sup>3+</sup>," *J. Chem. Phys.* **63**(5), 2074-2085 (1975).
  42. D.S. Moore, and J.C. Wright, "Laser spectroscopy of defect chemistry in CaF<sub>2</sub>: Er<sup>3+</sup>," *J. Chem. Phys.* **74**(3), 1626-1636 (1981).
  43. A. E. Nikiforov, A. Y. Zakharov, M. Y. Ugryumov, S. A. Kazanskii, A. I. Ryskin, and G. S. Shakurov, "Crystal fields of hexameric rare-earth clusters in fluorites," *Phys. Solid State* **47**(8), 1431-1435 (2005).
  44. S. Normani, L. Basyrova, P. Loiko, A. Benayad, A. Braud, A. Hideur, and P. Camy, "Mid-infrared laser operation of Er<sup>3+</sup>-doped BaF<sub>2</sub> and (Sr,Ba)F<sub>2</sub> crystals," *Opt. Lett.* **48**(2), 431-434 (2023).